Journal of
Ceramic Science
and Technology

J. Ceram. Sci. Technol., **08** [4] 485-492 (2017)
DOI: 10.4416/JCST2017-00024
available online at: http://www.ceramic-science.com

The Role of Pore-Formers on Grain Interior and Grain Boundary Conductivity in Tape-Cast Porous Sheets for Electrochemical Flue Gas Purification

C. Grings Schmidt, K.B. Andersen, E. Stamate, A. Kaiser, K. Kammer Hansen*

Department of Energy Conversion and Storage, Technical University of Denmark,
Frederiksborgvej 399, DK-4000 Roskilde, Denmark

received March 31, 2017; received in revised form July 2, 2017; accepted July 31, 2017

Abstract

$Ce_{0.9}Gd_{0.1}O_{1.95}$ (CGO) electrolytes for electrochemical flue gas purification were fabricated by means of tape casting with different types, shapes and sizes of pore-formers. The sintered bodies were characterized with electrochemical impedance spectroscopy, to investigate the role of the different pore-formers on the electrochemical properties of the cast tapes. A strong effect of the different pore-formers on the conductivity (both grain interior and grain boundary conductivities) was observed. In addition, the conductivity data were also correlated with previously obtained gas permeability data. The conductivity data correlated with the permeability data in the sense that a higher permeability lead to a lower conductivity. The porosity of the samples also influenced the conductivities. The higher the porosity of the sintered bodies, the lower the conductivity was, as expected.

Keywords: CGO, tape casting, EIS, conductivity

I. Introduction

Pollution from combustion of fossil fuels is a major problem. In the case of the exhaust gas from diesel engines, unwanted pollutants like particulate matter and nitrogen oxides, which are formed as a side product from N_2 and O_2 at high temperatures, are emitted. The nitrogen oxides are emitted primarily as nitric oxide, but also contain some nitrogen dioxide. Nitric oxide and nitrogen dioxide together are termed (NO_x). NO_x is problematic for human health and is a cause of acid rain and high local ozone concentrations [1,2]. Particulate matter is highly carcinogenic [3].

The cleanup of diesel exhaust gasses is therefore a subject of both great importance and interest. In order to remove the NO_x, an electrochemical reactor based on an oxide ionic-conducting electrolyte can be used. Such a reactor is, in its simplest form, made from a layer of a porous electrolyte between two porous electrodes as illustrated in Fig. 1. NO_x is reduced at the cathode to nitrogen and oxide anions when the reactor is polarized. The oxide anions are transported from the cathode to the anode through the electrolyte. At the anode, the oxide anions are either oxidized to oxygen or they react with the soot [4].

The pressure drop must be reduced across the reactor. In order to achieve this, the porosities of the different layers of reactor have to be controlled carefully.

If an electrochemical reactor for flue gas purification is used as a particulate filter, the gas permeability must be in the order of 10^{-11} to 10^{-12} m^2. Different methods to achieve porous structures have been described by Ohji *et al.*, which lead to different levels of gas permeability, depending on the processing and type of organic fugitives used [5]. It is well known that both the gas permeability and electrical conductivity of NO_X electrochemical filters are strongly dependent on microstructural parameters such as porosity, phase distribution and particle size [6–8]. In order to get the electrochemical reactor to function at low temperature, it must have a high conductivity. This leads to a compromise between gas permeability and conductivity.

A reactor for electrochemical flue gas purification can be made from alternating porous layers of an electronic-conducting oxide (e.g. a perovskite) electrode and an ionic-conducting electrolyte such as $Ce_{0.9}Gd_{0.1}O_{1.95}$ (CGO).

To obtain large ceramic sheets with good surface finish and thickness in the range 0.005 – 1.5 mm, tape casting can be used. Tape casting is a cost-effective way to make reactors for electrochemical flue gas purification with the above-mentioned structure with a suitable thickness. In order to make the reactors porous, pore-formers (PF) based on organic fugitives are often added to the tape-cast slurries. When the cast layers are sintered, the PF are burned out, giving rise to a porous structure.

A related work [9] has described the importance of porosity, pore size, pore connectivity and pore orientation on the gas permeability of thin, tape-cast CGO electrolyte layers for electrochemical NO_x filters prepared with different types of pore-former. Another related work [10] has described the influence of the same pore-formers on the mechanical properties of the thin tape-cast CGO electrolyte layers. However, the electrochemical properties, which are also of great importance for the electrochemical

* Corresponding author: kkha@dtu.dk

NO_x filters, might be affected when porosity and pore size are increased. Several studies on yttria-stabilized zirconia (YSZ) have illustrated that the level of porosity has a significant (negative) effect on ionic transport [11–14]. Ceria-based ceramics are expected to exhibit similar behavior [15]. Thus, it is of great interest and importance to study the influence of the different pore-formers on the electrochemical properties of porous CGO electrolyte layers. One way to characterize the influence of different pore-formers on the electrochemical properties is by employing the electrochemical impedance spectroscopy technique at low temperatures, as an essential investigative tool to resolve the intragranular (bulk) and intergranular (grain boundary) electrochemical properties [11,12,16]. The grain boundary component may include several microstructural defects (pores, cracks, grain boundaries) contributing to a blocking effect [17,18], although for denser, pure material, it is constituted primarily of the intrinsic grain boundary.

This study describes the influence of different pore-formers on the electrochemical properties of tape-cast and sintered ceramic structures of a porous CGO electrolyte for an electrochemical NO_x filter on the sintered microstructure of the CGO layer. For this purpose, pore-formers with different size and geometry (anisometry) were added to CGO tape-casting slurries. Then, the influence of the pore-former type (size and shape) on the electrochemical properties (ionic conductivity, activation energy, grain interior and grain boundary) of the sintered CGO layer was investigated. In addition, the conductivity values obtained in this study were also correlated with the gas permeability values obtained in the previous studies, in order to evaluate how these two properties are connected and understand how they could be controlled.

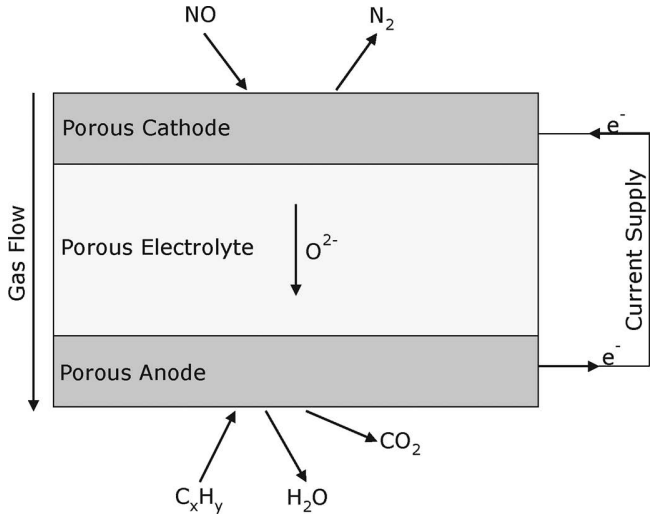

Fig. 1 : Schematic representation of an electrochemical flue gas purification cell.

II. Experimental

(1) Raw powders

The $Ce_{0.9}Gd_{0.1}O_{1.95}$ (CGO) used is an ultra-low surface area powder (ULSA-CGO GDC10-TC, Fuel Cell Materials, Lewis Center, USA, specific surface area of 6 m^2/g, d50: ~0.35 μm).

The five pore-formers used are:

1) Poly-methyl methacrylate micro-particles (PMMA MR10G, Esprix Technologies, Sarasota, FL, USA, d50: 10 μm)
2) Spherical graphite (AF 99.95, Graphit Kropfmühl AG, Hauzenberg, Germany, d50: 10 μm)
3) Spherical graphite (FormulaBT SLA1518, Superior Graphite, Chicago, IL, USA, d50: 17.7 μm)
4) Platelet graphite (SGB 10 L/99.9, Graphit Kropfmühl AG, Hauzenberg, Germany, d50: 10 μm)
5) Platelet graphite (FormulaBT LBG2025, Superior Graphite, Chicago, IL, USA, d50: 20.9 μm).

Data on the pore-formers provided by the supplier and the tapes they are used in are given in Table. 1. The short names for the pore-formers are: G = Graphite, SPH = Spherical, Plate = platelet-shaped.

(2) Slurry preparation and tape casting

For all five compositions of CGO tapes with pore-former, Table 1, the amount of the different pore-formers was kept constant at 23 vol%. In addition, the CGO and organic content were constant in all tapes. With the pore-former, the composition was 31.0 vol% CGO powder, 39 vol% binder and 7 vol% dispersant. Without a pore-former, the CGO to organic was the same, resulting in 54 vol% CGO with the same ratio of binder and dispersant as in the tapes with pore-formers.

Slurries for tape casting were prepared by dispersing the CGO powder in an azeotropic methylethylketone and ethanol mixture (MEKET) with polyvinylpyrrolidone (PVP), as described by Lobera *et al.* [19]. The slurries were ball-milled for 72 h at a speed of 220 rpm in PE bottles using zirconia balls. After milling, the particle size distribution (PSD) was bimodal with a particle size (d50) of approximately 0.35 μm. The pore-formers were then added to the slurries with additional dispersant. The slurries were ball-milled for 5 h at a low speed of 85 rpm. The particle size was measured after the milling to ensure the dispersion of the pore-former. Lastly, a PVB-based binder [20] system (mixture of binder, plasticizer and a release agent) was added to the slurries and allowed to rotate slowly for another 24 h.

Before casting, the slurry was filtered and de-aired. The suspensions were tape-cast with a 1.5-mm doctor blade height at a casting speed of 20 cm/min, resulting in a 310- to 430-μm sintered thickness. In a NO_x filter based on LSM/CGO (LSM: Strontium substituted lanthanum manganite) multilayers, each single CGO layer is normally tape-cast at a doctor blade clearance of 0.2 mm. The thick tapes CGO were made to achieve sufficiently mechanical strength to allow handling (transport, laser cutting, etc.) and to be able to perform the characterization with the methods described below (e.g. EIS).

(3) Characterization methods for tape-cast slurries and tapes

A laser diffraction particle size analyzer, LS13 320, Beckman Coultier, Brea, CA, USA, was used to measure particle size distributions. Quantachrome Autosorb 1 (Quantachrome GmbH & Co. KG, Odelzhausen, Germany)

was used to measure the specific surface area by means of gas adsorption measurements based on the BET method. The powders were degassed for 300 °C for 3 h and then the absorption with krypton gas was performed. Rheometer Haake RheoStress 600, Thermo Scientific, Germany, with parallel plate configuration and a gap of 0.1 mm between the plates, was used to measure the viscosity of the suspension before tape casting. Pore size distribution was measured by means of mercury porosimetry analysis (Quantachrome PoreMaster, Quantachrome GmbH & Co. KG, Odelzhausen, Germany).

A Hitachi TM3000, Hitachi High-Technologies Europe GmbH, Germany, tabletop SEM microscope was used to investigate the microstructure of the sintered porous CGO supports. The porous supports were mounted in epoxy and polished with a 1/4-micron diamond suspension before being examined in the scanning electron microscope.

(4) Sintering of porous tape-cast structures

The tape-cast green CGO sheets were cut to appropriate sizes to meet the requirements of the subsequent tests. The samples were slowly heated to a low temperature (< 800 °C) with a heating rate of 0.5 K/min to remove the organics and pore-former (debinding) and with 1 K/min to the sintering temperature. The samples were sintered in air for 4 h at a temperature of 1250 °C.

For the electrochemical impedance spectroscopy analysis, each 5 by 5 cm sintered sample was sputtered with a 100-nm layer of gold on both sides and finally laser cut into 6 by 6 mm samples.

(5) Electrochemical Impedance Spectroscopy (EIS)

The electrochemical measurements were conducted in a one-atmosphere setup that can contain up to four samples at a time. The cells were sandwiched between two gold meshes. In addition to this, a 100-nm gold layer was sputtered on both sides of the cells, which were laser-cut to 6 by 6 mm, before being mounted in the setup. To promote the contact between the cell and the gold mesh, the cells were loaded with 200 g weight. For the electrochemical measurements (impedance spectroscopy), a Gamry REF600 was used in standalone mode. The Gamry was controlled by Gamry software running in potentiostatic mode. The frequency range covered was 1 MHz to 1 mHz with ten points measured per decade, starting at high frequency. An amplitude of 36 mV RMS was used. The EIS measurements were performed at five temperatures; 100, 125, 150, 175 and 200 °C. All the measurements were performed in an atmosphere containing 20 % oxygen in argon. The flow rate was 100 mL/min. The gas composition was controlled with Brooks mass flow controllers.

(6) Gas permeability measurements

Permeation measurements were carried out using a locally in-built device as described by Schmidt *et al.* [9]. In short, the cells were placed in an appropriate cell house and pressure was applied to the cell, using pressurized air. The pressure difference was then measured.

III. Results and Discussion

(1) Properties and microstructure of porous CGO sheets

The relevant properties of tape-cast and sintered CGO layers prepared from five different types of pore-former for electrochemical NO_x filters based on LSM/CGO multilayers [21] were investigated; the results are summarized in Table 1.

Among all sintered PF-containing CGO layers, the PMMA sample has the lowest total porosity of about 40 % (including about 6 % closed porosity), the platelet graphite layer has a porosity of about 50 % and the two different tapes composed of spherical graphite also show a porosity of around 50 %.

For a microstructure analysis see [9].

Table 1: The properties (density and porosity) of porous CGO layers, prepared by tape casting of CGO slurries with different pore-formers. All formulations contain 22.99 vol% pore-former (despite the dense CGO layer) and were sintered at 1250 °C for 4 h.

Short name	Explanation	Specific Surface Area (m^2/g)	*Final Relative Density (%)	#Open Porosity (%)	##Closed Porosity (%)
Dense	No PF	None	86.1	7.3	6.6
PMMA	PMMA PF	0.518	58.6	34.9	6.5
G_Plate_10	Platelet graphite 10 µm PF	10.5	50.7	43.4	5.9
G_Plate_20	Platelet graphite 20 µm PF	4.9	51.4	44.0	4.6
G_SPH_10	Spherical graphite 10 µm PF	10.55	47.8	42.2	10.0
G_SPH_18	Spherical graphite 18 µm PF	6.6	52.2	34.8	13.0

*Density obtained from Hg porosimetry

#Porosity measured by means of Hg porosimetry

##Obtained from CP = 1 - FRD - OP, where CP is closed porosity, FRD is the final relative density and OP is the open porosity

(2) Electrochemical Impedance Spectroscopy (EIS)

The data were fitted using the PC-Windows program "Equivalent Circuit" by B.A. Boukamp [22]. The measured and fitted spectra recorded at 150 °C for the sample G_Plate_10 are shown in Fig. 2 as a typical example.

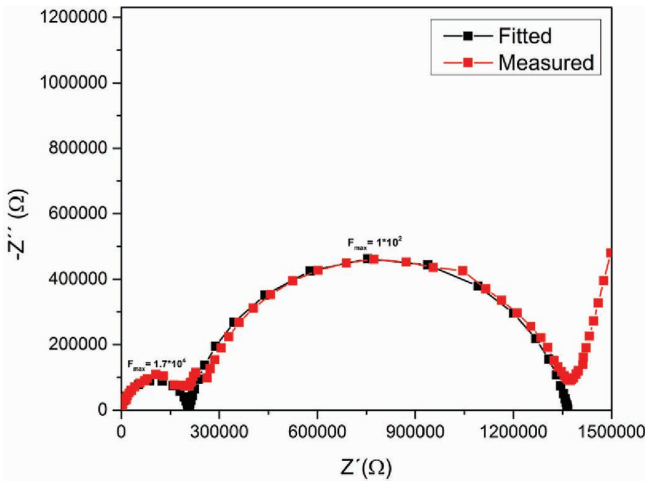

Fig. 2: Nyquist plot of the impedance spectra and fitting for the sample G_Plate_10 recorded at 150 °C.

A typical impedance spectrum (Fig. 2) reveals contributions that can be ascribed to the bulk, grain boundaries, and electrode processes based on differences in relaxation frequency and capacitance. It also shows that a good fit was achieved. As seen in Table 2, both bulk and grain-boundary contributions to the impedance are different for each pore-former used, which increases when the porosity is increased, which is in accordance to the results obtained by Pérez-Coll *et al.* [15]. In addition, the grain-boundary contribution is more dependent on the type of pore-former used than the bulk contribution.

The spectra for all samples were well separated into two well-defined arcs (microstructural contributions of grain interior and grain boundaries). A model consisting of 2 (RQ)'s in series was used in the fitting. As mentioned before, an electrode contribution was also observed, but neglected for the fitting. The high-frequency arc is due to the grain interior contribution and the low-frequency arc is due to the grain boundary contribution [23].

Q is a constant phase element with the admittance:

$$Y = Y_0(j\omega/\omega_0)^n, \quad (1)$$

where Y_0 and n are found from the fitting. ω is the cyclic frequency. In the fitting, the n values were allowed to vary freely. After fitting of all the data, the averages of the n-values were found. The n-values found in this study were very similar for all samples and temperatures recorded (among each frequency range) and an average of 0.96 was found for the low-frequency region while an average of 0.87 was found for the high-frequency region.

From the results of the fitting the near-equivalent capacitance, C_ω, and the summit frequency, F_{max}, were calculated using the equations [24]:

$$C_\omega = R^{(1-n)/n} Y_0^{1/n} \quad (2)$$

$$F_{max} = \frac{1}{2\pi}(RY_0)^{1/n} \quad (3)$$

The experimental values for resistance and capacitance of the bulk and grain boundary extracted from the impedance spectra were corrected for the macroscopic geometry factor of the sample (Ri·A and Ci/A, respectively). The values are given in Table 2.

From the resistances, the activation energies for the two processes were calculated. The values of the activation energies for the grain interior and the grain boundaries are given in Table 3.

The activation energies, summit frequencies, and n values are very similar for all the samples, which was expected as they are representatives of the same processes. The activation energies found for the grain interior (0.72 – 0.76 eV) and grain boundary (0.91 – 0.96 eV) conductivities are well in line with what was has previously been reported in the literature for bulk (0.72 – 0.73 eV) and grain boundary (0.87 – 0.91 eV) [15]. The average activation energy for the grain boundary was approximately 26 % higher than the activation energy for the grain interior and therefore confirms that the grain boundaries play a major role in the increase in activation energy of total conductivity at low temperatures. Furthermore, both the bulk and grain boundary activation energy are independent of porosity, as Table 3 shows.

(3) Gas permeability and porosity

A correlation between the gas permeability and conductivity can be seen in Fig. 3.

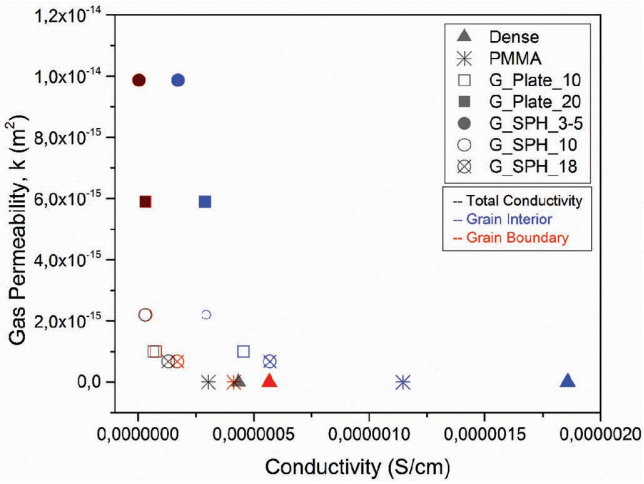

Fig. 3: Correlation between the gas permeability and bulk conductivity, grain boundary conductivity and total conductivity for the samples Dense, PMMA, G_SPH_10, G_SPH_18, G_Plate_10 and G_Plate_20.

Both the grain interior and the grain boundary conductivity change as a function of the pore-former. From Fig. 3, a good correlation between grain interior and grain boundary conductivity and the permeability is observed. A high permeability gives a low conductivity. The porosity also influences the conductivity. It is clear from Fig. 4 that a decrease in porosity results in an increasing total conductivity, as expected and confirmed in Table 2. The bulk conductivity is much higher than that of the grain boundary, and these differences get even bigger with a decrease in porosity.

Table 2: Resistances (Ω), capacities (F) and summit frequencies (Hz) for the two arcs for the cells Dense, PMMA, G_Plate_10, G_Plate_20, G_SPH_10 and G_SPH_18.

Dense	High frequency			Low frequency		
Temperature	R_1	C_1	F_{max}	R_2	C_2	F_{max}
100 °C	$2.7 \cdot 10^5$	$2.0 \cdot 10^{-10}$	$2.9 \cdot 10^3$	$2.1 \cdot 10^6$	$2.0 \cdot 10^{-8}$	3.7
125 °C	$6.0 \cdot 10^4$	$2.0 \cdot 10^{-10}$	$1.3 \cdot 10^4$	$2.9 \cdot 10^5$	$1.9 \cdot 10^{-8}$	$2.9 \cdot 10^1$
150 °C	$1.7 \cdot 10^4$	$2.0 \cdot 10^{-10}$	$4.9 \cdot 10^4$	$5.5 \cdot 10^4$	$1.9 \cdot 10^{-8}$	$1.6 \cdot 10^2$
175 °C	$5.7 \cdot 10^3$	$2.0 \cdot 10^{-10}$	$1.4 \cdot 10^5$	$1.4 \cdot 10^4$	$2.0 \cdot 10^{-8}$	$6.1 \cdot 10^2$
200 °C	$1.8 \cdot 10^3$	$2.2 \cdot 10^{-10}$	$4.1 \cdot 10^5$	$3.9 \cdot 10^3$	$1.9 \cdot 10^{-8}$	$2.2 \cdot 10^3$

PMMA	High frequency			Low frequency		
Temperature	R_1	C_1	F_{max}	R_2	C_2	F_{max}
100 °C	$4.9 \cdot 10^5$	$1.6 \cdot 10^{-10}$	$2.1 \cdot 10^3$	$2.4 \cdot 10^6$	$1.1 \cdot 10^{-8}$	6.1
125°C	$1.2 \cdot 10^5$	$1.6 \cdot 10^{-10}$	$8.5 \cdot 10^3$	$4.2 \cdot 10^5$	$1.1 \cdot 10^{-8}$	$3.6 \cdot 10^1$
150 °C	$3.0 \cdot 10^4$	$1.5 \cdot 10^{-10}$	$3.5 \cdot 10^4$	$8.3 \cdot 10^4$	$1.0 \cdot 10^{-8}$	$1.9 \cdot 10^2$
175 °C	$1.1 \cdot 10^4$	$1.5 \cdot 10^{-10}$	$1.0 \cdot 10^5$	$2.1 \cdot 10^4$	$1.1 \cdot 10^{-8}$	$7.1 \cdot 10^2$
200 °C	$3.9 \cdot 10^3$	$1.5 \cdot 10^{-10}$	$2.7 \cdot 10^5$	$6.3 \cdot 10^3$	$1.1 \cdot 10^{-8}$	$2.3 \cdot 10^3$

G_Plate_10	High frequency			Low frequency		
Temperature	R_1	C_1	F_{max}	R_2	C_2	F_{max}
100 °C	$1.3 \cdot 10^6$	$1.3 \cdot 10^{-10}$	$1.0 \cdot 10^3$	$1.6 \cdot 10^7$	$3.2 \cdot 10^{-9}$	3.4
125 °C	$2.8 \cdot 10^5$	$1.3 \cdot 10^{-10}$	$4.8 \cdot 10^3$	$2.5 \cdot 10^6$	$3.3 \cdot 10^{-9}$	$2.2 \cdot 10^1$
150 °C	$8.3 \cdot 10^4$	$1.3 \cdot 10^{-10}$	$1.7 \cdot 10^4$	$5.3 \cdot 10^5$	$3.3 \cdot 10^{-9}$	$1.0 \cdot 10^2$
175 °C	$2.9 \cdot 10^4$	$1.3 \cdot 10^{-10}$	$4.7 \cdot 10^4$	$1.4 \cdot 10^5$	$3.2 \cdot 10^{-9}$	$4.1 \cdot 10^2$
200 °C	$1.2 \cdot 10^4$	$1.2 \cdot 10^{-10}$	$1.3 \cdot 10^5$	$3.9 \cdot 10^4$	$3.4 \cdot 10^{-9}$	$1.4 \cdot 10^3$

G_Plate_20	High frequency			Low frequency		
Temperature	R_1	C_1	F_{max}	R_2	C_2	F_{max}
100 °C	$1.5 \cdot 10^6$	$1.3 \cdot 10^{-10}$	$8.4 \cdot 10^2$	$3.0 \cdot 10^7$	$2.5 \cdot 10^{-9}$	2.1
125 °C	$3.4 \cdot 10^5$	$1.3 \cdot 10^{-10}$	$3.7 \cdot 10^3$	$4.3 \cdot 10^6$	$2.5 \cdot 10^{-9}$	$1.5 \cdot 10^1$
150 °C	$9.8 \cdot 10^4$	$1.3 \cdot 10^{-10}$	$1.3 \cdot 10^4$	$8.3 \cdot 10^5$	$2.1 \cdot 10^{-9}$	$9.3 \cdot 10^1$
175 °C	$2.8 \cdot 10^4$	$1.2 \cdot 10^{-10}$	$4.6 \cdot 10^4$	$1.9 \cdot 10^5$	$2.4 \cdot 10^{-9}$	$3.4 \cdot 10^2$
200 °C	$1.1 \cdot 10^4$	$1.2 \cdot 10^{-10}$	$1.3 \cdot 10^5$	$4.9 \cdot 10^4$	$2.4 \cdot 10^{-9}$	$1.3 \cdot 10^3$

G_SPH_10	High frequency			Low frequency		
Temperature	R_1	C_1	F_{max}	R_2	C_2	F_{max}
100 °C	$2.0 \cdot 10^6$	$1.2 \cdot 10^{-10}$	$6.4 \cdot 10^2$	$3.8 \cdot 10^7$	$1.5 \cdot 10^{-9}$	2.8
125 °C	$4.6 \cdot 10^5$	$1.3 \cdot 10^{-10}$	$2.7 \cdot 10^3$	$6.0 \cdot 10^6$	$1.5 \cdot 10^{-9}$	$1.7 \cdot 10^1$
150 °C	$1.3 \cdot 10^5$	$1.3 \cdot 10^{-10}$	$1.0 \cdot 10^4$	$1.1 \cdot 10^6$	$1.5 \cdot 10^{-9}$	$1.0 \cdot 10^2$
175 °C	$3.9 \cdot 10^4$	$1.3 \cdot 10^{-10}$	$3.1 \cdot 10^4$	$2.8 \cdot 10^5$	$1.4 \cdot 10^{-9}$	$4.1 \cdot 10^2$
200 °C	$1.6 \cdot 10^4$	$1.2 \cdot 10^{-10}$	$8.3 \cdot 10^4$	$7.6 \cdot 10^4$	$1.4 \cdot 10^{-9}$	$1.5 \cdot 10^3$

G_SPH_18	High frequency			Low frequency		
Temperature	R_1	C_1	F_{max}	R_2	C_2	F_{max}
100 °C	$9.5 \cdot 10^5$	$1.3 \cdot 10^{-10}$	$1.3 \cdot 10^3$	$5.9 \cdot 10^6$	$6.3 \cdot 10^{-9}$	4.3
125 °C	$2.3 \cdot 10^5$	$1.3 \cdot 10^{-10}$	$5.3 \cdot 10^3$	$1.0 \cdot 10^6$	$6.2 \cdot 10^{-9}$	$2.5 \cdot 10^1$
150 °C	$6.7 \cdot 10^4$	$1.3 \cdot 10^{-10}$	$1.8 \cdot 10^4$	$2.2 \cdot 10^5$	$6.5 \cdot 10^{-9}$	$1.1 \cdot 10^2$
175 °C	$2.3 \cdot 10^4$	$1.3 \cdot 10^{-10}$	$5.6 \cdot 10^4$	$5.2 \cdot 10^4$	$6.1 \cdot 10^{-9}$	$5.0 \cdot 10^2$
200 °C	$8.5 \cdot 10^3$	$1.2 \cdot 10^{-10}$	$1.5 \cdot 10^5$	$1.7 \cdot 10^4$	$6.5 \cdot 10^{-9}$	$1.4 \cdot 10^3$

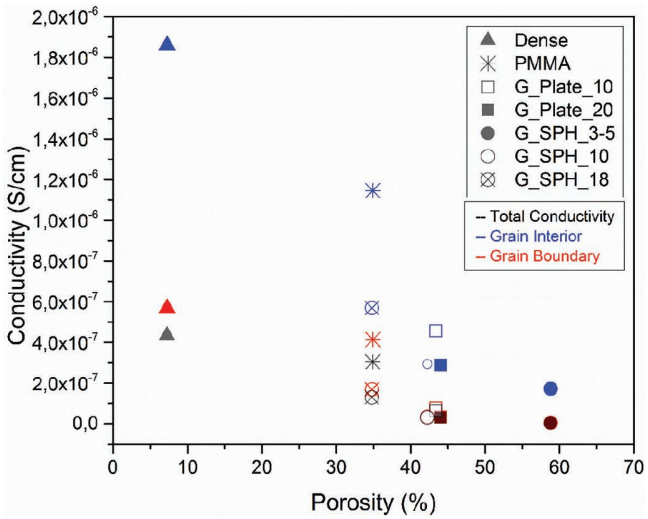

Fig. 4: Correlation between porosity and bulk conductivity, grain boundary conductivity and total conductivity for the samples Dense, PMMA, G_SPH_10, G_SPH_18, G_Plate_10 and G_Plate_20.

The grain boundary conductivity will be strongly dependent on the connectivity of the individual grains and therefore strongly dependent on the microstructure of the sample. A high permeability is due to a more open structure with fewer contact points between the grains. This is confirmed by the SEM micrographs. The more open the porosity is, the lower is the conductivity. This also implies that when a filter unit is designed, both the porosity and conductivity have to be taken into account, and the final filter unit is designed against the background of a tradeoff between the two parameters. The fact that the grain interior conductivity also changes with the pore-former is due to the effect of the porosities. The grain interior conductivity is determined with Bruggeman's asymmetric model [25], that is it will be affected by the porosities.

Table 3: Activation energies for the two arcs for the cells Dense, PMMA, G_Plate_10, G_Plate_20, G, G_SPH_10 and G_SPH_18.

Activation energy	High Frequency (Intragranular)	Low Frequency (Intergranular)
Dense	0.76 eV	0.96 eV
PMMA	0.74 eV	0.91 eV
G_Plate_10	0.72 eV	0.91 eV
G_Plate_20	0.75 eV	0.96 eV
G_SPH_10	0.74 eV	0.94 eV
G_SPH_18	0.73 eV	0.91 eV

IV. Summary and Conclusions

The influence of porosity, introduced by the use of different pore-formers during tape casting, on the electrochemical properties of sintered porous CGO layers for electrochemical NO_x filters has been investigated.

Distinct differences have been observed in the grain interior and grain boundary conductivities of CGO tape-cast layers made with different pore-formers. Activation energy values were similar to those found in the literature for grain interior and grain boundaries, and the values did not depend on the pore-former used or the porosity of the samples. On the other hand, the conductivity shows a dependence on the porosity and gas permeability.

References

1 Butler, A.R.,Williams, D.L.H.: The physiological-role of nitric-oxide, *Chem. Soc. Rev.*, **22**, 233–241, (1993).

2 Manahan, S.: Environmental chemistry, 1994, *Ann Arbor, MI Lewis Publ.*, (n.d.).

3 Wei, E.T., Shu, H.P.: Nitroaromatic carcinogens in diesel soot: A review of laboratory findings, *Am. J. Public Health*, **73**, [9], 1085–1088, (1983).

4 Pancharatnam, S.: Catalytic decomposition of nitric oxide on zirconia by electrolytic removal of oxygen, *J. Electrochem. Soc.*, **122**, [7], 869, (1975).

5 Ohji, T., Fukushima, M.: Macro-porous ceramics: processing and properties, *Int. Mater. Rev.*, **57**, 115–131, (2012).

6 Clemmer, R.M.C., Corbin, S.F.: Influence of porous composite microstructure on the processing and properties of solid oxide fuel cell anodes, *Solid State Ionics*, **166**, 251–259, (2004).

7 Chen, X.J., Khor, K.a., Chan, S.H., Yu, L.G.: Influence of microstructure on the ionic conductivity of yttria-stabilized zirconia electrolyte, *Mater. Sci. Eng. A*, **335**, 246–252, (2002).

8 Min Park, Y., Man Choi, G.: Microstructure and electrical properties of YSZ-NiO composites, *Solid State Ionics*, **120**, 265–274, (1999).

9 Schmidt, C.G., Andersen, K.B., Fu, Z., Hansen, K.K., Roosen, A., Kaiser, A.: Effect of pore formers on properties of tape cast porous sheets for electrochemical flue gas purification, *J. Eur. Ceram. Soc.*, **36**, 645–653, (2016).

10 Charlas, B., Schmidt,C.G., Frandsen, H.L., Andersen, K.B., Bocaccini, D., Hansen, K.K., Roosen, A., Kaiser, A.: Influence of pore former on porosity and mechanical properties of tape-cast $Ce_{0.9}Gd_{0.1}O_{1.95}$ electrolytes for electrochemical flue gas purification, *Ceram. Int.*, **42**, 4546–4555, (2016).

11 Schouler, E.J.L., Mesbahi, N., Vitter, G.: *In situ* study of the sintering process of yttria stabilized zirconia by impedance spectroscopy, *Solid State Ionics*, **9–10**, 989, (1983).

12 Badwal, S.P.S., Drennan, J.: Yttria-zirconia: effect of microstructure on conductivity, *J. Mater. Sci.*, **22**, 3231, (1987).

13 Steil, M.C., Thevenot, F., Kleitz, M.: Densification of yttria-stabilized zirconia: impedance spectroscopy analysis, *J. Electrochem. Soc.*, **144**, 390, (1997).

14 Gibson, I.R., Dransfield, G.P., Irvine, J.T.S.: Sinterability of commercial 8 mol% yttria-stabilized zirconia powders and the effect of sintered density on the ionic conductivity, *J. Mater. Sci.*, **33**, 4297, (1998).

15 Pérez-Coll, D., Sánchez-López, E., Mather, G.C.: Influence of porosity on the bulk and grain-boundary electrical properties of Gd-doped ceria, *Solid State Ionics*, **181**, 1033–1042, (2010).

16 Badwal, S.P.S., Drennan, J.: Evaluation of conducting properties of yttria-zirconia wafers, *Solid State Ionics*, **40**, 869, (1990).

17 Dessemond, L., Muchillo, R., Hénault, M., Kleitz, M.: Electric conduction-blocking effects of voids and 2nd phases in stabilized zirconia, *J. Appl. Phys. A*, **57**, 57, (1993).

18 de Florio, D.Z. Muchillo, R.: Sintering of zirconia-yttria ceramics studied by impedance spectroscopy, *Solid State Ionics*, **123**, 301, (1999).

19 Lobera, M.P., Serra, J.M., Foghmoes, S.P., Søgaard, M., Kaiser, A.: On the use of supported ceria membranes for oxyfuel process/syngas production, *J. Memb. Sci.*, **385–386**, 154–161, (2011).

[20] Klemensø, T., Menon, M., Ramousse, S.: Low toxicity binder systems for tape cast $Ce_{0.9}Gd_{0.1}O_{1.95}$ laminates, *Ceram. Int.*, **36**, 773 – 780, (2010).

[21] Schmidt, C.G., Ippolito, D., Bentzen, J.J., Andersen,K.B., Kaiser, A. Hansen, K.K.: Fabrication and characterization of multi-layer ceramics for electrochemical flue gas purification, *J. Electrochem. Soc.*, **160**, [9], E113 – E119, (2013).

[22] Boukamp, B.A.: A nonlinear least-squares fit procedure for analysis of immitance data of electrochemical systems, *Solid State Ionics*, **20**, 31, (1986).

[23] MacDonald, J.R.: Impedance Spectroscopy: Emphasizing Solid Materials and Systems. Wiley-Interscience, New York, 1987.

[24] Jacobsen, T., Zachau-Christiansen, B., Bay, L., Skaarup, S.: No Title; p. 29 in Proc. 17th Int. Symp. Mater. Sci. High Temp. Electrochem. Ceram. Met. Edited by F.W. Poulsen and E. Al. Roskilde, 1996.

[25] Bruggeman, D.A.G.: Calculation of various physical constants of heterogeneous substances. I. Dielectricity constants and conductivities of mixed bodies from isotropic substances (in German), *Ann. Phys.*, **24,** 636, (1935).